Imaging Delamination in Composite Laminates Using Perturbation to Steady-state Wavefields

Wei Xu[1,2,3*], Maosen Cao[1,3], Zhongqing Su[2], Hao Xu[4],

Maciej Radzieński[5], Wiesław Ostachowicz[5]

[1] Department of Engineering Mechanics, Hohai University, Nanjing 210098, People's Republic of China

[2] Department of Mechanical Engineering, The Hong Kong Polytechnic University, Hung Hom, Kowloon, Hong Kong, People's Republic of China

[3] Jiangsu Province Wind Power Structural Engineering Research Center, Hohai University, Nanjing 210098, People's Republic of China

[4] School of Aeronautics and Astronautics, Faculty of Vehicle Engineering and Mechanics, State Key Laboratory of Structural Analysis for Industrial Equipment, Dalian University of Technology, Dalian 116024, People's Republic of China

[5] Institute of Fluid-Flow Machinery, Polish Academy of Sciences, Gdańsk 80-231, Poland

[*]To whom correspondence should be addressed

E-mail addresses: wxu@hhu.edu.cn (W. Xu); cmszhy@hhu.edu.cn (M. Cao); zhongqing.su@polyu.edu.hk (Z. Su); xuhao@dlut.edu.cn (H. Xu); maciej.radzienski@imp.gda.pl (M. Radzieński); wieslaw.ostachowicz@imp.gda.pl (W. Ostachowicz)

Abstract: Delamination in composite laminates, though barely visible, can jeopardize integrity and safety of the composite structures. Interaction of guided waves with delamination in full wavefields have been widely used to graphically characterize the delamination. Recently, steady-state wavefields (SWs) in place of transient wavefields have been used for imaging delamination. However, interaction with delamination can be largely obscured by steady-state waves and become barely visible. Addressing this problem, this study proposes a novel approach for imaging delamination using perturbation to SWs. In particular, a new concept of delamination-caused perturbation to a SW is proposed. Compared to scattered waves from delamination, it is determined by delamination only and naturally sensitive to delamination. Delamination-caused perturbation to a SW is concentrated within the delamination region and rapidly attenuates at undamaged locations. On the basis of this new concept, a delamination index (DI) is established for imaging delamination, by which the delamination can be graphically characterized. The capability of the approach is experimentally validated on composite laminates with delamination, whose SWs are acquired through laser scanning. The experimental results validate that delamination imaging can be achieved by DIs, by which the occurrence, location, and size of the delamination can be graphically characterized.

***Keywords*:** composite laminate; delamination; steady-state wavefield; laser scanning; wavenumber filtering; delamination index

1 Introduction

Delamination in composite laminates, though barely visible, can jeopardize integrity and safety of the composite structures, such as wind turbine blades. With this concern, there is a great need to detect delamination in the early stage.

Interaction of guided waves with defects in full wavefields can graphically characterize the occurrence, locations, and sizes of the defects [1]. In the recent three decades, with the aid of advanced non-contact measurement techniques, mainly the laser scanning using a scanning laser vibrometer (SLV), structural transient wavefields (TWs) can be accurately acquired with high spatial resolutions for damage visualization [2-4]. Scanning in a structural region of interest, lasers can serve as sensors to pointwisely acquire structural responses [3-35] or serve as actuators to pointwisely excite the structure [35-43]. Besides laser scanning, digital image correlation with high-speed cameras [44] can acquire full wavefields. For better visualization of damage, the frequency-wavenumber filtering [45] was adopted to isolate damage-caused scattered waves from incident waves [6]. The wavenumber approaches have been widely adopted and developed [7,9-11,13-36,40-44,46]. Besides, other approaches using curvelet [12] and wavelet [39] have been proposed for processing wavefield data. The literature on damage visualization relying on wavefields were comprehensively reviewed and compared in Refs. [17,27].

Amongst the studies on structural damage visualization relying on wavefields acquired through laser scanning, delamination imaging has attracted the most attention. Representative studies are as follows. Sohn *et al.* [9,10] presented signal and image processing algorithms for automatical delamination detection of composite laminates. Michaels *et al.* [11] used the frequency-wavenumber domain analysis to

remove source waves and isolate scattered waves from delamination of composite laminates. Rogge and Johnston [13] presented a method for analyzing ultrasonic wavefield by calculating the continuous wavelet transform of the wavefield data in the spatial domain, whereby the wavenumber spectrum can be determined for delamination detection. Rogge and Leckey [14] presented a local Fourier domain analysis method for processing wavefield data, by which the delamination depth can be determined. Flynn and Jarmer [16] used a single-tone excitation to acquire steady-state wavefield (SW) for delamination visualization of composite laminates. Comparison of the local wavenumber mapping and acoustic wavenumber spectroscopy was performed [26]. The approach was then expanded to an aluminum panel using multi-tone excitations [18]. Flynn *et al.* [40] proposed a method for imaging delamination using local estimates of wavenumbers, which is capable of producing detailed images of impact delamination in a complicated composite component. Tian *et al.* [19,22] investigated interaction of waves with delamination. Different wavenumbers compared to a pristine case can be used for quantitative evaluation of delamination. Mesnil *et al.* [24] reported the application of both instantaneous and local wavenumber damage quantification techniques to wavefield data for delaminated composite laminates from a simple single delamination case to a more complex multi-ply delamination case. Juarez and Leckey [25] presented a new methodology based on multi-frequency local wavenumber analysis for quantitative assessment of multi-ply delamination damage in carbon fiber reinforced polymer (CFRP) composite laminates. An [41] presented a technique of impact-delamination visualization by the zero-lag cross-correlation imaging, which can physically isolate and visualize only the standing wave feature from the measured ultrasonic wavefields. Williams *et al.* [28] developed a model for estimating scattering of a circular defect

and compared scattering estimates for both artificial and impact delamination. Esfandabadi *et al.* [29] presented a damage detection and localization technique based on a compressive sensing algorithm, which can significantly reduce the acquisition time without losing accuracy of delamination detection. Kudela *et al.* [30] used the wavenumber adaptive image filtering and signal processing of full wavefield data for delamination visualization and assessment of composite laminates. Wave scattering and mode conservation at delamination were clearly observed.

More recently, SWs in place of TWs have been used for damage visualization in both metallic and composite plates [16,18,26,34]. Compared to TWs, the benefits of using SWs are threefold [16]: first, magnitudes of SWs can be enhanced because energy is effectively "pumped" into structures, producing high signal to noise ratios of wavefields; second, a delay to allow an excitation wave to "die out" can be avoided; third, measurement time at each point can be reduced because fewer cycles are needed [16]. In a physical sense, as incident waves can be trapped in delamination to form standing waves [9], interaction of waves with delamination can be enhanced when harmonic excitations are applied on composite laminates to generate SWs. Considering a plate under a transverse harmonic excitation, which bears a delamination in its center. In its TW, scattered waves from the delamination can be observed (figure 1(a)); however, in its SW, interaction with the delamination can be largely obscured by steady-state waves and become barely visible (figure 1(b)). In this situation, conventional processing approaches such as the wavenumber filtering are insufficient. Thereby, the key to using SWs for damage visualization is to extract time-invariant properties of waves that are sensitive to delamination [16]. Addressing this problem, this study proposes a novel approach for imaging delamination using perturbation to SWs. In particular, a new concept of delamination-caused perturbation

to a SW is proposed. Compared to scattered waves from delamination, it is determined by delamination only and naturally sensitive to delamination. Delamination-caused perturbation to a SW exist within the delamination region and vanish at undamaged locations. On the basis of this new concept, a delamination index (DI) is established for imaging delamination, by which the occurrence, location, and size of the delamination can be graphically characterized.

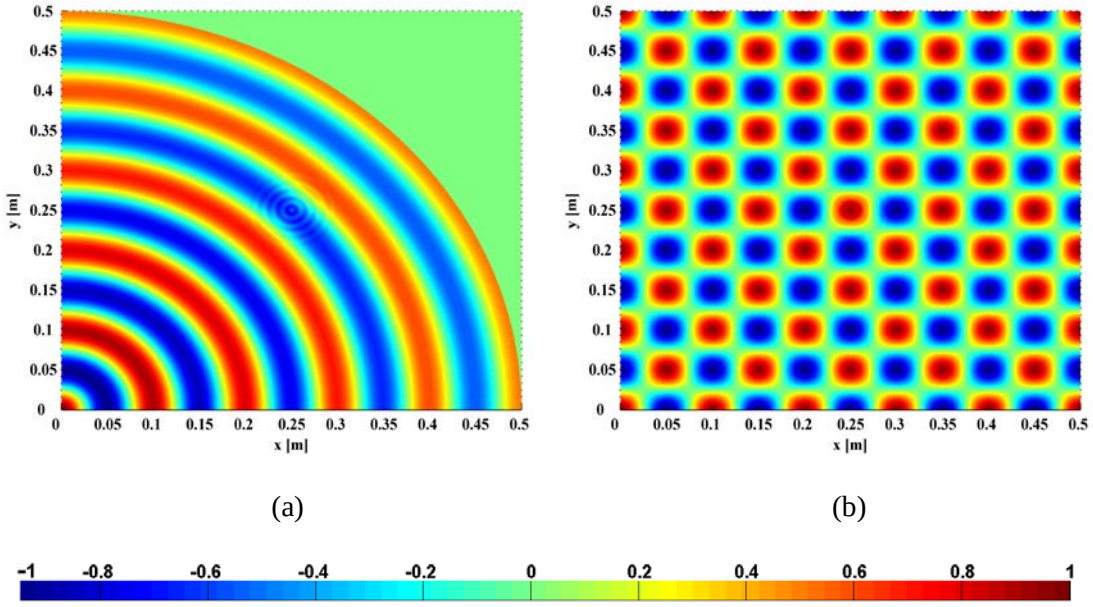

Figure 1 Snapshots of the (a) TW and (b) SW of the plate under the transverse harmonic excitation.

Note that when the excitation frequency decreases to the category of low-frequency vibration, SWs become operating deflection shapes at the excitation frequencies. Vibration-based approaches have been widely developed for delamination detection of composite laminates, such as the vibro-acoustic [47-51], linear discriminant analysis [52,53], local resonance [54], curvature [55-58], Teager-Kaiser energy [59,60], fuzzy logic [61] and frequency domain-based correlation [62] approaches. Recently, the artificial intelligence approaches [63-66]

have attracted increasing attention, which are considered to be promising for applications to real-world composite structures.

The rest of the paper is organized as follows. Starting from the equation of transverse motion of a cross-ply composite laminate, Section 2 proposes a novel approach for imaging delamination using perturbation to SWs. Section 3 experimentally validates the approach on a CFRP laminate with a delamination. The CFRP laminate is excited by harmonic waves generated by a lead-zirconate-titanate (PZT) piezoelectric actuator, and its SWs are acquired through laser scanning using a SLV. Section 4 presents concluding remarks.

2 Delamination-caused perturbation to SWs

Assume that a cross-ply composite laminate is under a transverse harmonic excitation, which is applied outside the inspection region of the composite laminate. Its waveforms from measurement points at scanning grids are denoted as $w(x,y,t)$, where x and y are coordinates in the *x*- and *y*-directions and t is time. By the Fourier transform, the $w(x,y,t)$ maps from the space-time domain to the space-frequency domain, whereby the SW $W(x,y)$ at the excitation frequency f_e can be obtained [34]:

$$W(x,y)=\int_{-\infty}^{\infty} w(x,y,t)e^{-\mathrm{i}2\pi ft}\,\mathrm{d}t\Big|_{f=f_e}, \tag{1}$$

where i denotes imaginary unit.

To remove noise components involved in a SW, instead of the conventional "point-by-point" manner, the SW is inspected in a "region-by-region" manner [67] in this study: the SW is averaged in a scaled Gaussian windowing function $\bar{g}_s(x,y)$ that slides inside the SW data, by which the multiscale SW $W_s(x,y)$ is formed:

$$\bar{W}(u,v,s)=\frac{1}{s}W\otimes\bar{g}_s(u,v), \tag{2a}$$

$$W_s(x,y)=\bar{W}(u,v,s)\Big|_{\substack{u=x\\v=y}}, \tag{2b}$$

where $\bar{g}_s(x,y)=\frac{1}{s}g(\frac{-x}{s},\frac{-y}{s})$ with the Gaussian function $g(x,y)=(2/\pi)^{1/2}e^{-(x^2+y^2)}$ and scale parameter s, and $\otimes$ denotes convolution. The multiscale SW exhibits an intrinsic multiscale property, whose merits are twofold as follows [68]. On the one hand, noise components caused by sensors and environments are inevitably involved in the measured SWs. By gradually increasing scale parameters, noise components are averaged in ever-wider Gaussian windows. When the scales increase to satisfising levels, noise components in the SWs are basically eliminated. On the other hand, delamination-caused perturbation to the SWs are retained with increasing scale parameters for imaging delamination. Thereby, multiscale SWs are beneficial to imaging delamination of composite laminates under noisy conditions.

In the inspection region of a cross-ply composite laminate made of 0/90° orientations, regarding the elements bearing no transverse excitation, the equation of transverse motion of the elements can be written as [69]

$$D_{11}\frac{\partial^4 W_s(x,y)}{\partial x^4}+2(D_{12}+2D_{66})\frac{\partial^4 W_s(x,y)}{\partial x^2\partial y^2}+D_{22}\frac{\partial^4 W_s(x,y)}{\partial y^4}+(2\pi f_e)^2\bar{\rho}\frac{\partial^2 W_s(x,y)}{\partial t^2}=0, \tag{3}$$

where $\bar{\rho}=\sum_{d=1}^{M}\rho^{(d)}(z_d-z_{d-1})$ is the average density of the composite laminate per unit area of the midsurface with $\rho^{(d)}$ being the density of the dth lamina per unit volume. Considering a composite laminate bearing a local delamination in a region denoted as Ω, reduction in stiffness will be caused by the delamination [70]. The stiffness coefficients $D_{ij}(x,y)$ of the composite laminate can be represented as

$$D_{ij}(x,y)=\begin{cases} D_{ij}^{I} & x,y\notin\Omega \\ D_{ij}^{D} & x,y\in\Omega \end{cases}, \tag{4}$$

where superscripts I and D indicate the intact and damaged statuses, respectively.

By substituting equation (4) into equation (3), we have

$$D_{11}^{I}\frac{\partial^4 W_s(x,y)}{\partial x^4}+2(D_{12}^{I}+2D_{66}^{I})\frac{\partial^4 W_s(x,y)}{\partial x^2\partial y^2}+D_{22}^{I}\frac{\partial^4 W_s(x,y)}{\partial y^4}-(2\pi f_e)^2\overline{\rho}^{I}W_s(x,y)=P_D(x,y), \tag{5}$$

where $P_D(x,y)$ represents the delamination-caused perturbation to the SW:

$$P_D(x,y)=\begin{cases} 0 & x,y\notin\Omega \\ \Delta\mathbf{D}_D\cdot\boldsymbol{\Theta}(W_s(x,y))-\omega^2\Delta\overline{\rho}W_s(x,y) & x,y\in\Omega \end{cases}, \tag{6}$$

in which $\Delta_D\mathbf{D}=(D_{11}^{I}-D_{11}^{D},(D_{12}^{I}+2D_{66}^{I})-(D_{12}^{D}+2D_{66}^{D}),D_{22}^{I}-D_{22}^{D})$ denotes stiffness change vector and $\boldsymbol{\Theta}(\bullet)=(\frac{\partial^4}{\partial x^4},\frac{2\partial^4}{\partial x^2\partial y^2},\frac{\partial^4}{\partial y^4})$.

For some practical composite structures in service, structural and material parameters of composite laminates can be unknown. In these situations, it is barely possible to directly obtain $P_D(x,y)$ by equation (5). To deal with this problem, equation (5) is further re-written by simplifying the stiffness coefficients:

$$D_{11}^{I}\frac{\partial^4 W_s(x,y)}{\partial x^4}+2D_{11}^{I}\frac{\partial^4 W_s(x,y)}{\partial x^2\partial y^2}+D_{11}^{I}\frac{\partial^4 W_s(x,y)}{\partial y^4}-(2\pi f_e)^2\overline{\rho}^{I}W_s(x,y)=P_D(x,y)+P_M(x,y), \tag{7}$$

where $P_M(x,y)$ called the material-caused perturbation is additionally generated:

$$P_M(x,y)=\Delta\mathbf{D}_M\cdot\boldsymbol{\Theta}(W(x,y)), \tag{8}$$

in which $\Delta\mathbf{D}_M=(0,D_{11}^{I}-D_{12}^{I}-2D_{66}^{I},D_{11}^{I}-D_{22}^{I})$. Note that equation (7) represents the equation of motion of a "pseudo" isotropic laminated plate with one stiffness coefficient D_{11}^{I}. Delamination-caused perturbation $P_D(x,y)$ exist in the in the delamination region whereas material-caused perturbation $P_M(x,y)$ exist over the

whole inspection region. Without losing generality, equation (7) is divided by D_{11}^{I}, whereby normalized perturbation to the SW can be obtained, denoted as $P^{*}(x,y)$:

$$P^{*}(x,y)=P_{D}^{*}(x,y)+P_{M}^{*}(x,y)=\frac{\partial^{4}W_{s}(x,y)}{\partial x^{4}}+2\frac{\partial^{4}W_{s}(x,y)}{\partial x^{2}\partial y^{2}}+\frac{\partial^{4}W_{s}(x,y)}{\partial y^{4}}-\lambda^{4}W_{s}(x,y), \tag{9}$$

where $P_{D}^{*}(x,y)=\frac{P_{D}(x,y)}{D_{11}^{I}}$ and $P_{M}^{*}(x,y)=\frac{P_{M}(x,y)}{D_{11}^{I}}$ are normalized $P_{D}(x,y)$ and $P_{M}(x,y)$, respectively, and $\lambda^{4}=\frac{(2\pi f_{e})^{2}\overline{\rho}^{I}}{D_{11}^{I}}$ is the constant related to the structural and material parameters and excitation frequency. For a real-world composite laminate with unknown structural and material parameters, its constant λ^{4} cannot be directly obtained. Addressing this problem, the λ^{4} is estimated in a statistic manner in this study by calculating and analyzing the point-wise $\lambda^{4}(x,y)$ for each measurement point [71]:

$$\lambda^{4}(x,y)=\nabla^{4}W_{s}(x,y)/W_{s}(x,y), \tag{10}$$

where ∇^{4} denotes $\frac{\partial^{4}}{\partial x^{4}}+2\frac{\partial^{4}}{\partial x^{2}\partial y^{2}}+\frac{\partial^{4}}{\partial y^{4}}$. The $\lambda^{4}(x,y)$ with the maximum probability can be regarded as the λ^{4}. Therefore, the approach proposed in this study for imaging delamination in composite laminates is baseline-free, which means that material or structural parameters can be absent.

The wavenumber analysis [6] is adopted in this study to isolate two types of components in $P^{*}(x,y)$, *i.e.*, $P_{D}^{*}(x,y)$ and $P_{m}^{*}(x,y)$. As these two components are in the forms of "waves" at the excitation frequency, hereafter in this study they are named D-mode and M-mode perturbation waves, respectively. It is noteworthy that in a physical sense D-mode perturbation waves are generated by delamination; in

contrast, the M-mode perturbation waves are “pseudo” because they are generated due to the manner of simplifying stiffness coefficients of the composite laminate in equation (7). The wavenumber spectrum $\hat{P}^*(k_x,k_y)$ can be obtained by transforming the $P^*(x,y)$ to the wavenumber domain using the Fourier transform:

$$\hat{P}^*(k_x,k_y)=\int_{-\infty}^{\infty}\int_{-\infty}^{\infty}P^*(x,y)e^{-\mathrm{i}2\pi(k_x x+k_x y)}\,\mathrm{d}x\,\mathrm{d}y, \tag{11}$$

where k_x and k_y are wavenumbers in the *x*- and *y*-directions, respectively. To isolate the M-mode perturbation waves $P_M^*(x,y)$ from $P^*(x,y)$, a low-pass wavenumber filter $F(x,y)$ based on a Tukey window is designed:

$$F(k_x,k_y)=F_x(k_x)F_y(k_y), \tag{12a}$$

$$F_x(k_x)=\begin{cases}1 & |k_x|<\tilde{k}_x\\ \dfrac{1}{2}\left[1+\cos\dfrac{\pi(k_x-\tilde{k}_x)}{\alpha\tilde{k}_x}\right] & \tilde{k}_x\le|k_x|\le(1+\alpha)\tilde{k}_x\\ 0 & |k_x|>(1+\alpha)\tilde{k}_x\end{cases}, \tag{12b}$$

$$F_y(k_y)=\begin{cases}1 & |k_y|<\tilde{k}_y\\ \dfrac{1}{2}\left[1+\cos\dfrac{\pi(k_y-\tilde{k}_y)}{\alpha\tilde{k}_y}\right] & \tilde{k}_y\le|k_y|\le(1+\alpha)\tilde{k}_y\\ 0 & |k_y|>(1+\alpha)\tilde{k}_y\end{cases}. \tag{12c}$$

where $\tilde{k}_x$ and $\tilde{k}_y$ represent upper limitations of M-mode perturbation waves in the *x*- and *y*-directions, respectively, and cutoff parameter α is 0.1 in this study. Thereby, $P_M^*(x,y)$ can be isolated from $P^*(x,y)$ by the inverse Fourier transform:

$$P_M^*(x,y)=\frac{1}{4\pi^2}\int_{-\infty}^{\infty}\int_{-\infty}^{\infty}F(k_x,k_y)\hat{P}(k_x,k_y)e^{\mathrm{i}2\pi(k_x x+k_x x)}\,\mathrm{d}k_x\,\mathrm{d}k_y. \tag{13}$$

Hence, D-mode perturbation waves $P_D^*(x,y)$ can be obtained by subtracting $P_M^*(x,y)$ from $P^*(x,y)$:

$$P_D^*(x,y) = P^*(x,y) - P_M^*(x,y). \tag{14}$$

A delamination index (DI) can be established using the normalized modulus of $P_D^*(x,y)$, denoted as $DI(x,y)$:

$$DI(x,y) = \left|P_D^*(x,y)\right| / \max\left|P_D^*(x,y)\right|. \tag{15}$$

Theoretically, the DI exists in the delamination region only and vanishes at undamaged locations. In practice, the DI cannot completely vanish at undamaged locations due to uncertainties during measurements; instead, it rapidly attenuates at undamaged locations. Thereby, delamination imaging can be achieved by the planform of the DI, whereby the occurrence, location, and size of the delamination can be graphically characterized. Note that the existing damage detection approaches using SWs basically rely on signal processing such as filtering to extract damage features from SWs. In the aspect of physical sense, the proposed approach can be superior to existing approaches because it builds on equilibrium of a SW, perturbation of which in a physical sense is naturally sensitive to delamination.

For easy comprehension, the flowchart and schematic of the approach for imaging delamination are illustrated in figure 2 and figure 3, respectively.

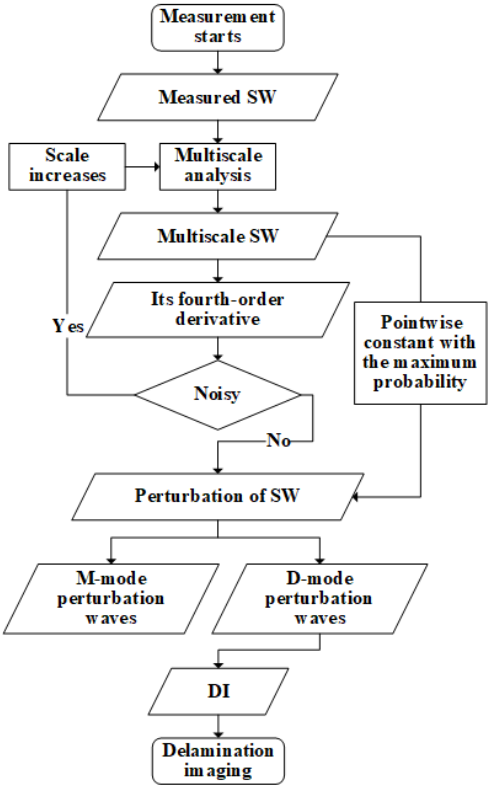

Figure 2 Flowchart of the approach for imaging delamination.

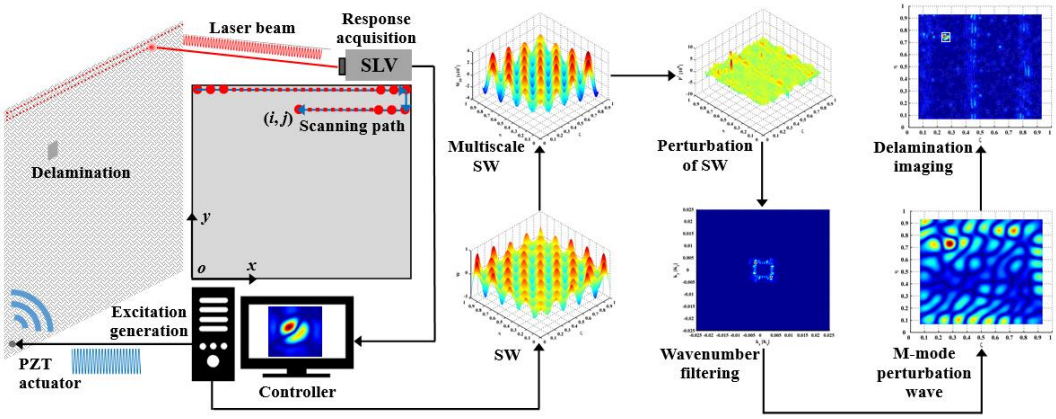

Figure 3 Schematic of the approach for imaging delamination.

3 Imaging delamination using perturbation to SWs

The capability of the approach is experimentally validated on three specimens of composite laminates with delamination (Specimens I, II, and III), whose SWs are acquired through laser scanning using a SLV.

3.1 Experimental setup

The experimental setup is shown in figure 4, which consists a SLV (Polytec PSV-400) and an arbitrary waveform generator (Agilent 33250A). In this study, the scheme of piezoelectric actuation/laser sensing is adopted because it can provide higher energy in wavefields than other actuation/sensing schemes [35]. As illustrated in figure 3, the PZT is controlled by the arbitrary waveform generator to generate harmonic waves. Amplitudes of the harmonic excitations are proportional to the input voltages of the arbitrary waveform generator. In this study, the voltages for the three specimens are all 1 V. The entire scanning region is meshed by $N_y \times N_x$, which consists N_x and N_y uniform sampling points in each row and column in the *x*- and *y*-directions, respectively. Velocity responses of the $N_y \times N_x$ measurement points are pointwisely measured using a SLV to form the waveforms and wavefields. The measured responses are averaged five times for smoothing. The schematic of point-wise scanning measurement is illustrated in figure 3 with the zoomed-in view of the scanning path and measurement points. Without losing generality, SWs in this study are normalized with their maximum magnitudes being unit.

In this study, steady-state waves at 1 to 10 kHz are used to stimulate interaction with the delamination. To “pump” more energy into composite laminates for larger magnitudes of their SWs, natural frequencies associated with out-of-plane modes are selected as excitation frequencies for the specimens.

Full laser scanning for the specimens in this study requires up to several hours depending on the SW sizes, which can encounter difficulties for practical applications to real-world composite structures if their SWs need to be densely sampled. Although densely sampled SWs are to the benefit of imaging small delamination, superfluous sampling points makes the full laser scanning time-consuming; in addition, noise

interference can be amplified in derivatives of SWs [72]. Fast laser scanning strategy using a continuously scanning laser Doppler vibrometer is a promising technology to measure SWs in a short time [58].

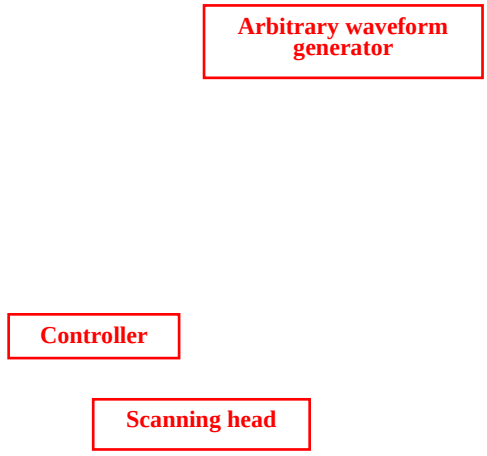

Figure 4 Experimental setup.

3.2 Experimental results for Specimen I

A CFRP symmetric cross-ply laminate made of 0/90º orientations is taken as the Specimen I, shown in figure 5. The specimen consists of four plies and has the lengths L_x and L_y of 500 mm in the *x*- and *y*-directions, respectively, and thickness h of 1.5 mm in the *z*-direction. When Specimen I was fabricated a delamination (15 mm × 15 mm) was manufactured by inserting a square Teflon sheet between the interfaces of the second ply and the third ply. The delamination is centered at *x*=125 mm and *y*=375 mm, spanning from 117.5 mm to 132.5 mm, 367.5 mm to 382.5 mm in the *x*- and *y*-directions, respectively. In dimensionless coordinates, the delamination is centered at $\zeta = 0.25$ and $\eta = 0.75$, spanning from 0.235 to 0.265, 0.735 to 0.765 in the $\zeta -$ and $\eta -$directions, respectively. The surface of the specimen is totally flat, and the delamination region is barely visible from its appearance even in a zoomed-in version. The outside surface of the first ply is defined as the front surface of the specimen, and the other side of the specimen is the back surface. Outlines of the

delamination region are marked in white on the front surface for illustration. The specimens in this study are suspended by two strings in its two upper corners to approximate free boundary conditions for simplicity and repeatability of experiments [73]. A circular lead-zirconate-titanate (PZT) actuator with the diameter of 10 mm is mounted at the lower left corner on the front surface. The back surface of the specimen is covered by reflection tapes to enhance laser reflection.

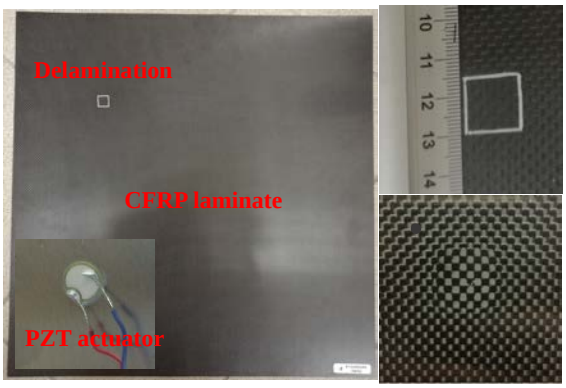

Figure 5 Specimen I: CFRP laminate with a Teflon-caused delamination.

After modal analysis over a broad frequency range [74], natural frequencies of the CFRP laminate at 2256.3, 2723.4, 3504.7, and 3923.4 Hz are arbitrarily selected as excitation frequencies for Specimen I. Corresponding SWs (figure 6) are measured from 371 × 371 measurement points through laser scanning, which are used for imaging delamination, regarded as Scenarios I, II, III, and IV of Specimen I, respectively. To eliminate noise interference, the SWs $W(x, y)$ are convoluted with the scaled Gaussian window by equation (2). The scale parameter s is increased to a satisfising level until $\nabla^4 W_s(x, y)$ becomes smooth. For the SWs in this study, the satisfising scale parameters are found to be 30 after trials. Corresponding multiscale SWs are shown in figure 7 with success in removal of noise interference.

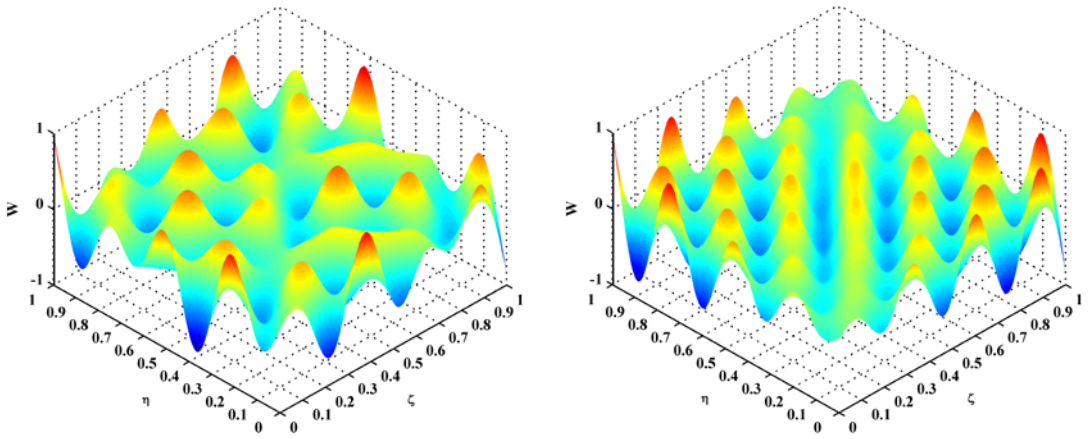

(a) (b)

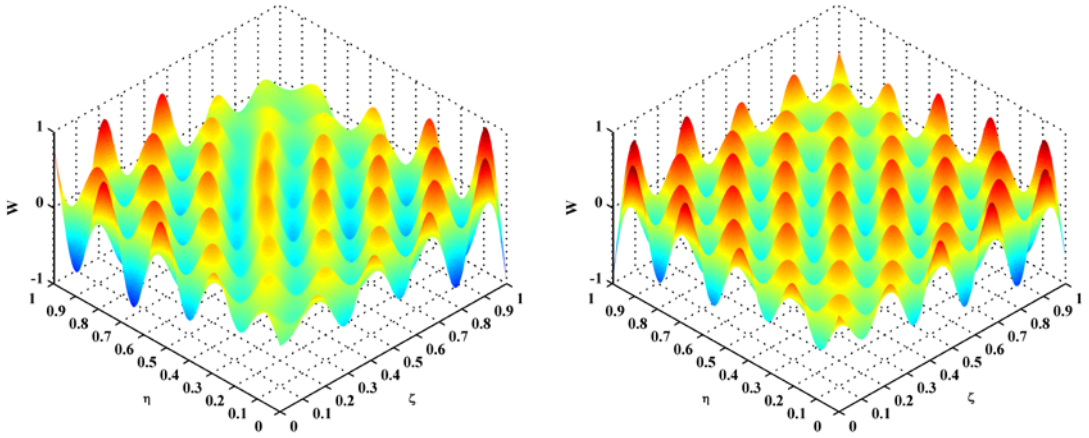

(c) (d)

Figure 6 SWs for Scenarios (a) I, (b) II, (c) III, and (d)IV.

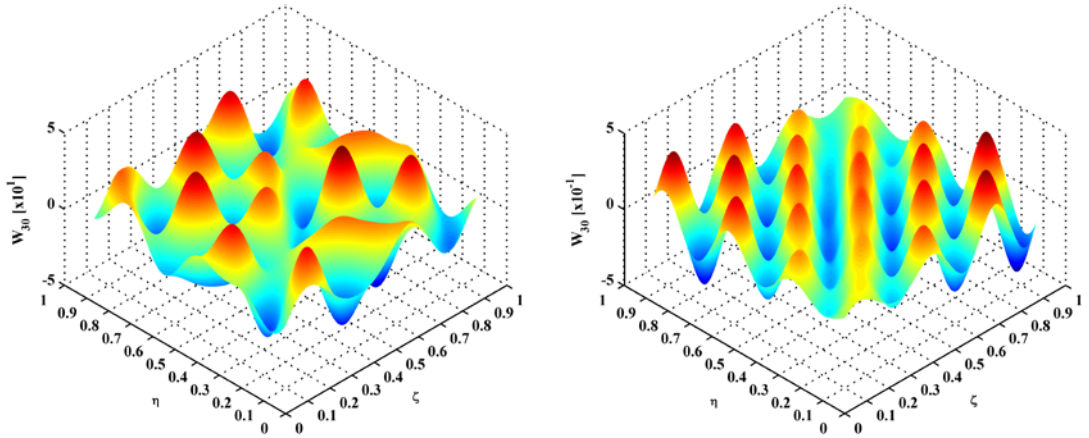

(a) (b)

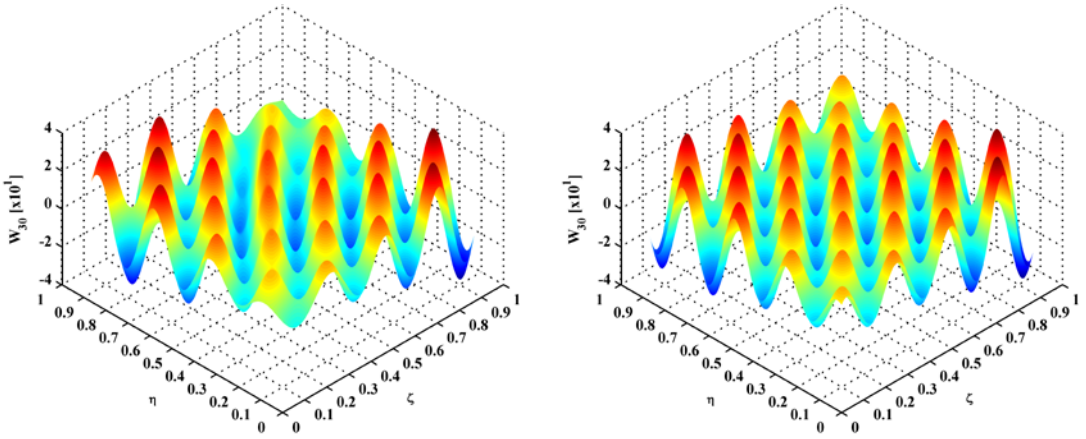

(c) (d)

Figure 7 Multiscale SWs for Scenarios (a) I, (b) II, (c) III, and (d) IV.

By equation (10), the point-wise constants $\lambda^4(x,y)$ are calculated and shown in figure 8. Sorted into 1000 uniform sections, $\lambda^4(x,y)$ being 9.65×10^6, 1.62×10^7, 2.68×10^7, and 3.35×10^7 with the maximum counts (indicated by red dashed lines) are regarded as the constants λ^4 for Scenarios I, II, III, and IV, respectively. By substituting the λ^4 into equation (9), normalized perturbation $P^*(x,y)$ of the SWs for Scenarios I, II, III, and IV are obtained and shown in figure 9(a), (b), (c), and (d), respectively. In each $P^*(x,y)$, a sharply-rising peak appears in the delamination region, and fluctuant waves distributed in the whole inspection region can be also observed. Thereby, the D-mode perturbation waves can be used for imaging delamination whereas M-mode perturbation waves can cause interference: the peaks in the delamination regions are determined by the D-mode perturbation waves, which are concentrated in the delamination regions only and rapidly attenuate when propagating out the delamination region. However, M-mode perturbation waves propagate over the whole inspection regions, resulting in interference in delamination imaging.

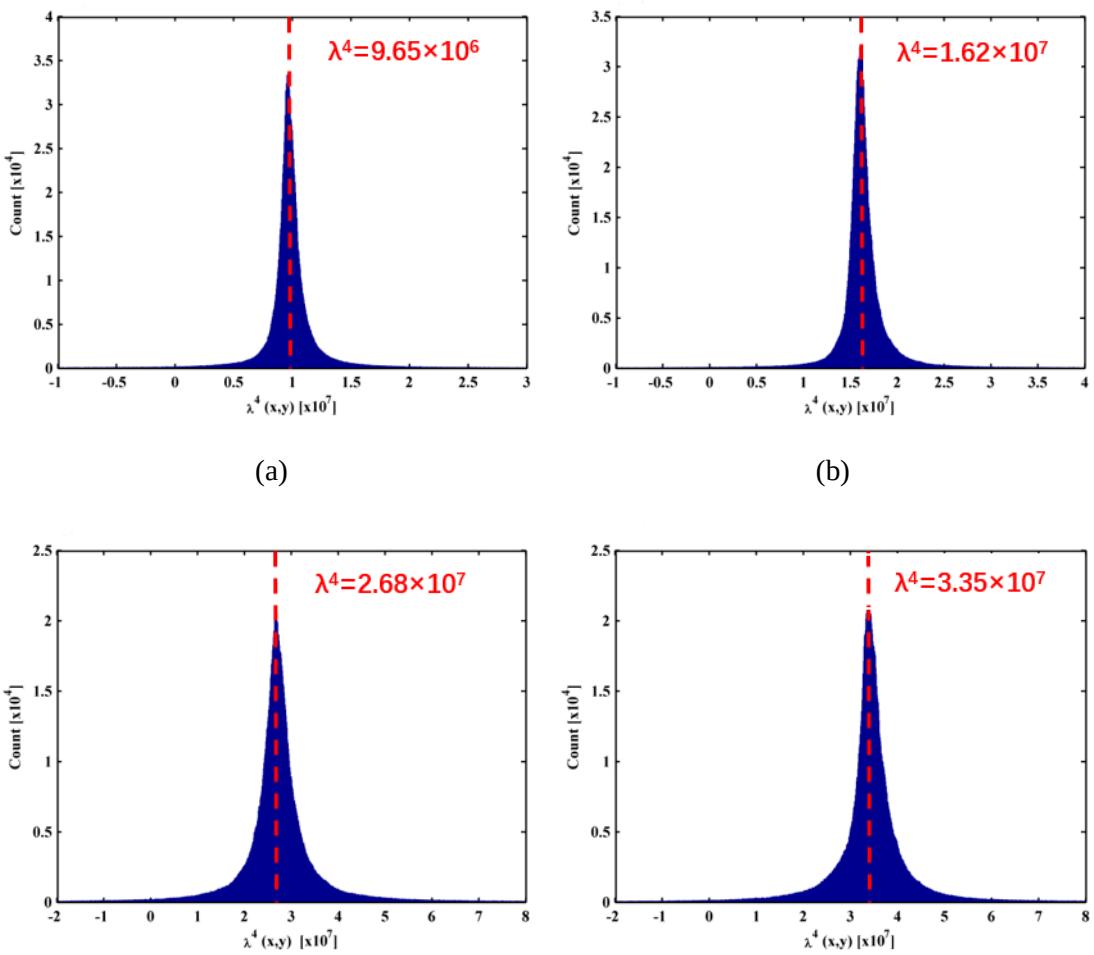

(a) (b)

(c) (d)

Figure 8 Distribution of $\lambda^4(x, y)$ for Scenarios (a) I, (b) II, (c) III, and (d) IV.

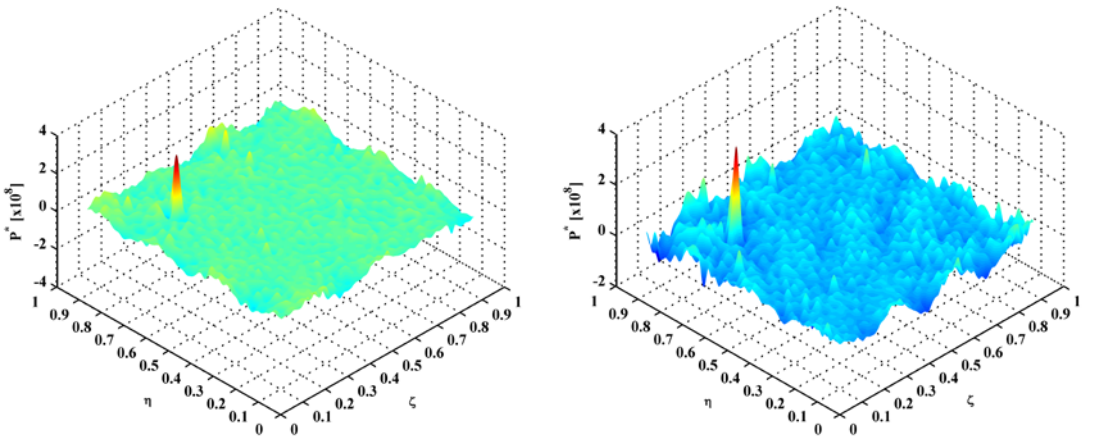

(a) (b)

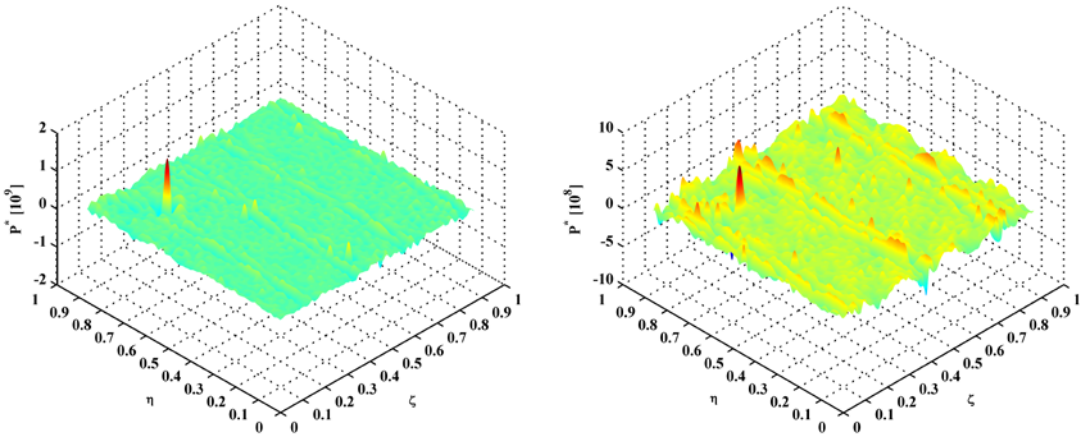

(c) (d)

Figure 9 Perturbation to SWs for Scenarios (a) I, (b) II, (c) III, and (d) IV.

By equation (11), $P^*(x,y)$ are transformed to $\hat{P}^*(k_x,k_y)$ in the wavenumber domain by the fast Fourier transform and shown in figure 10, with wavenumbers k_x and k_y in the *x*- and *y*-directions, respectively. Without losing generality, wavenumbers k_x and k_y in this study are divided by the spatial sampling frequencies $K_x=(N_x-1)/L_x$ and $K_y=(N_y-1)/L_y$ in the *x*- and *y*-directions, respectively. It can be seen from figure 10 that M-mode and D-mode perturbation waves have distinct distributions in the wavenumber domain: M-mode perturbation waves are distributed at lower wavenumbers in shapes of square boxes, which correspond to the directions of steady-state wave propagation in the *x*- and *y*-directions; in contrast, D-mode perturbation waves are distributed at higher wavenumbers in the regions surrounding the M-mode perturbation waves. To isolate the M-mode perturbation waves, the wavenumber filtering is applied by equation (12), by which the filtered $\hat{P}^*(k_x,k_y)$ are shown in figure 11. By equation (13), the M-mode perturbation waves are reconstructed by inverse fast Fourier transform. Showing in figure 12, the moduli of the M-mode perturbation waves are distributed

over the whole inspection region with higher magnitudes near the boundaries.

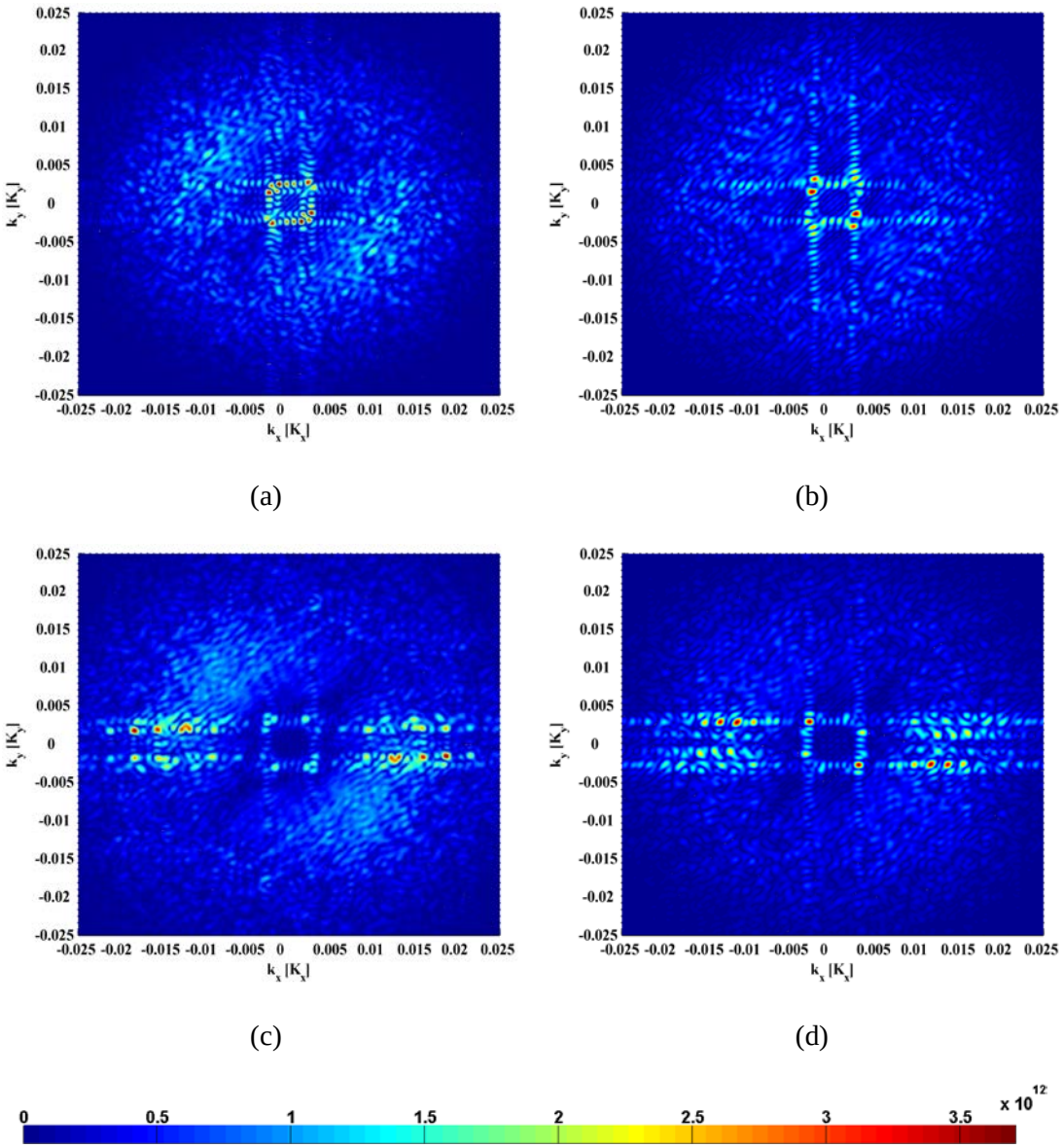

Figure 10 Perturbation in the wavenumber domain for Scenarios (a) I, (b) II, (c) III, and (d) IV.

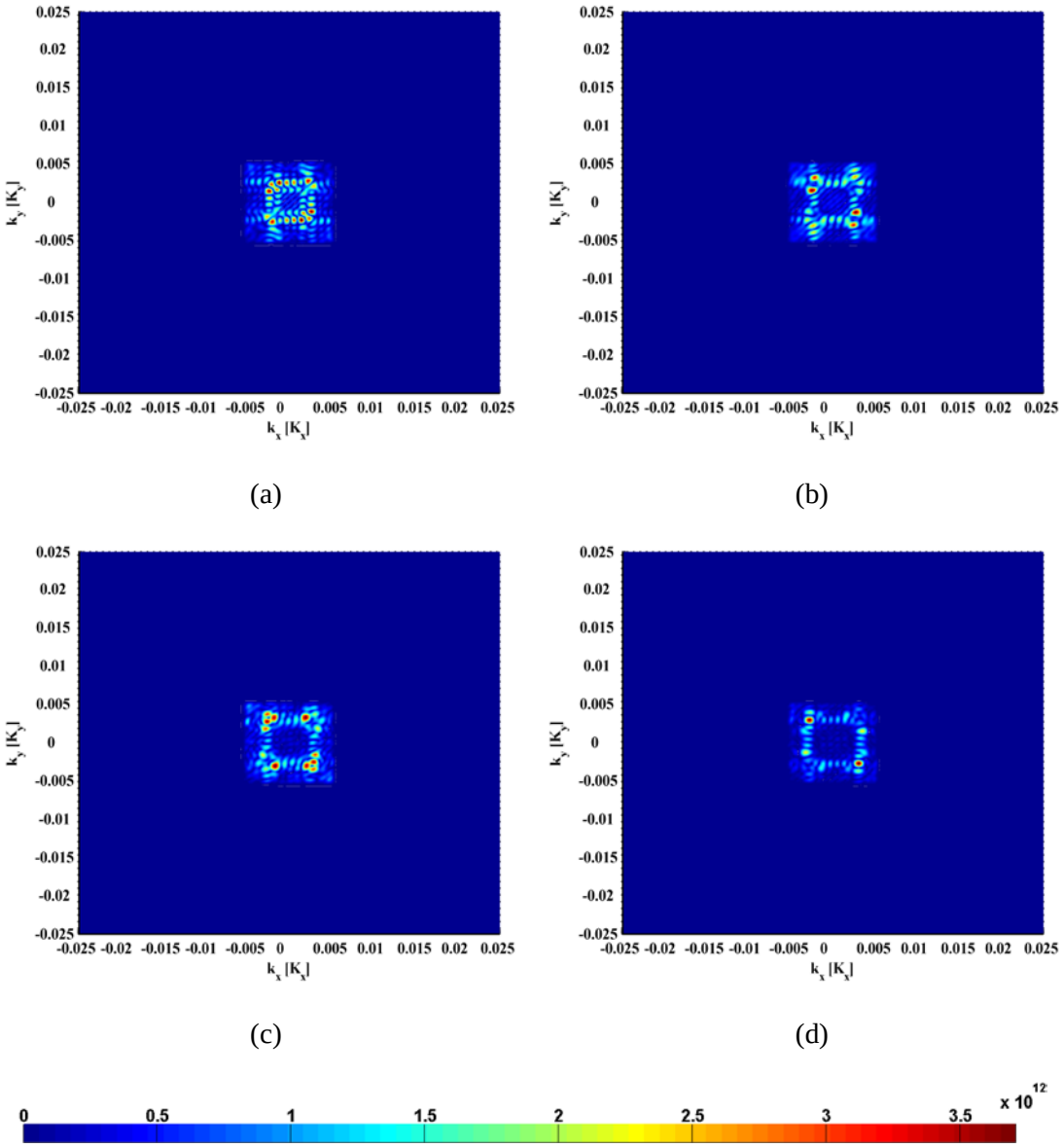

Figure 11 Filtered perturbation in the wavenumber domain for Scenarios (a) I, (b) II, (c) III, and (d) IV.

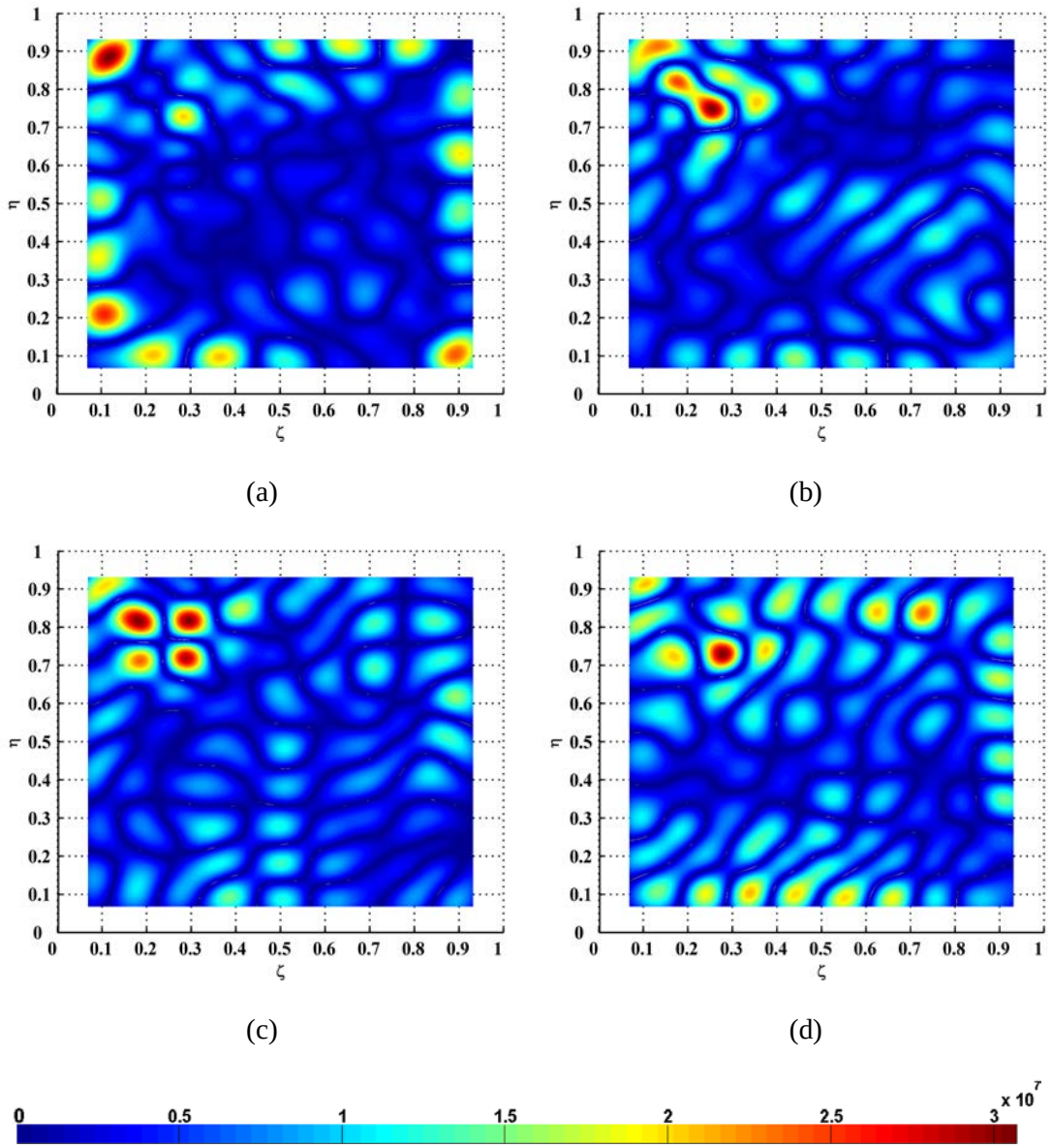

Figure 12 Moduli of M-mode perturbation waves for Scenarios (a) I, (b) II, (c) III, and (d) IV.

By equation (14), D-mode perturbation waves $P_D^*(x,y)$ can be obtained by subtracting $P_M^*(x,y)$ from $P^*(x,y)$, on the basis of which the DIs are obtained by equation (15) and shown in figure 13. It can be seen from figure 13 that in each DI a peak concentrated in the delamination region graphically characterize the delamination: the detected delamination is centered at $\zeta = 0.25$ and $\eta = 0.75$, spanning from about 0.235 to 0.265, 0.735 to 0.765 in the $\zeta-$ and $\eta-$directions,

respectively. The results of delamination imaging correspond to the actual region of the delamination whose outlines are marked in white. To clearly visualize the imaging details of the delamination, zoomed-in views of the regions surrounding the delamination are shown in figure 14. The experimental results validate that delamination imaging can be achieved by the approach proposed in this study, by which the occurrence, location, and size of the delamination can be graphically characterized.

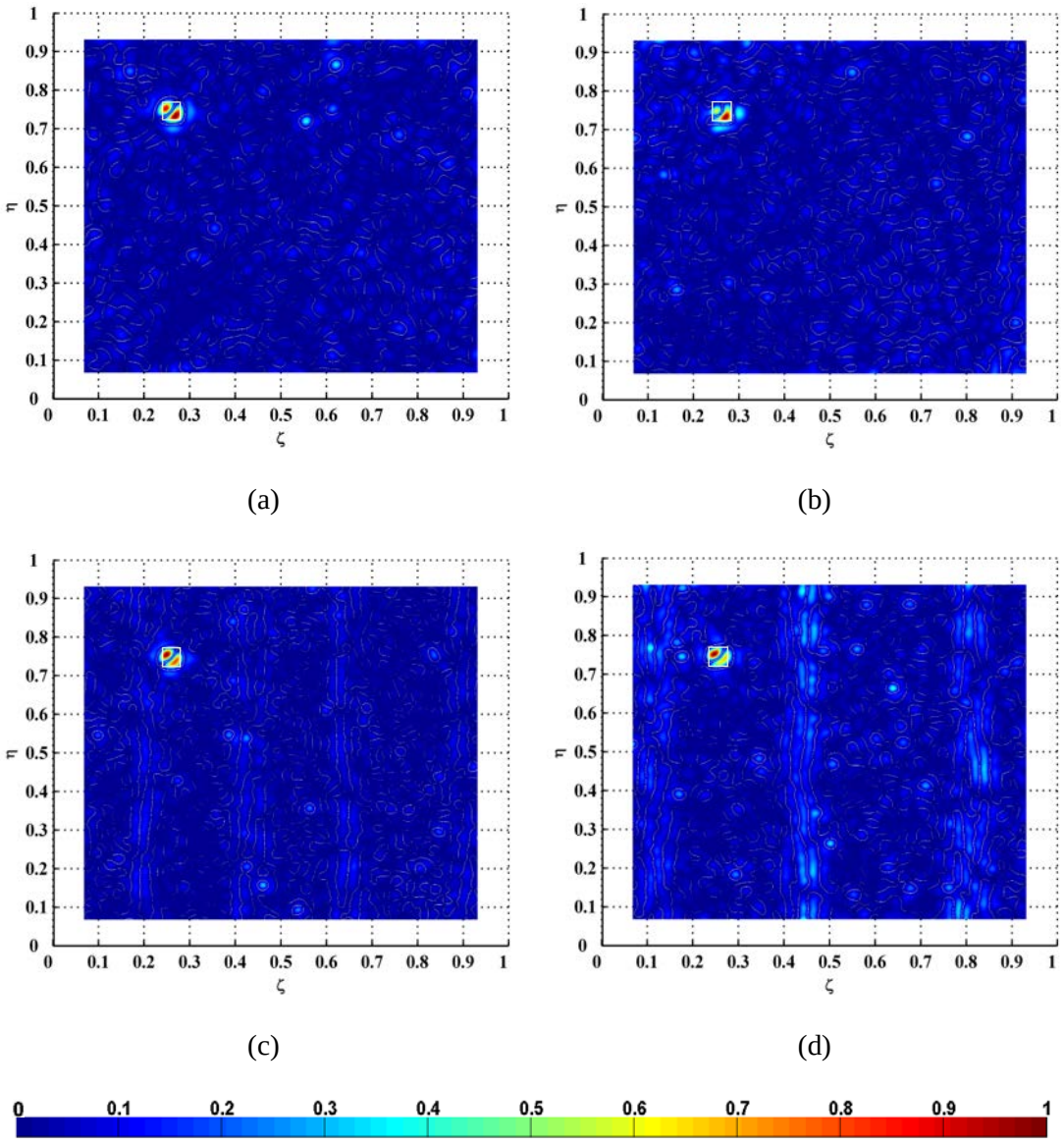

Figure 13 DIs for Scenarios (a) I, (b) II, (c) III, and (d) IV.

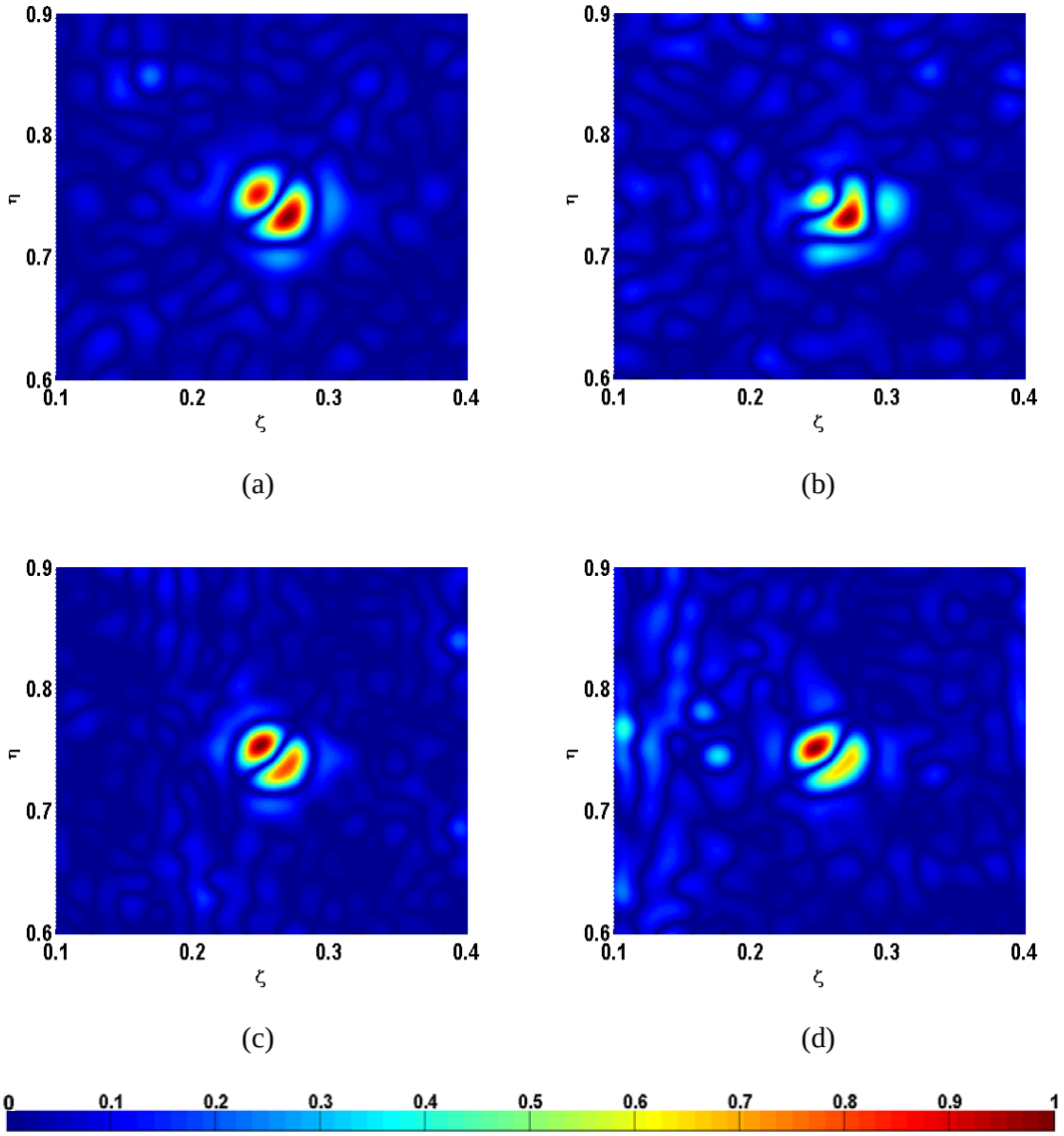

Figure 14 Zoomed-in views of DIs for Scenarios (a) I, (b) II, (c) III, and (d) IV.

3.3 Experimental results for Specimen II

To validate the feasibility of the approach to delamination with different depths, an eight-ply cross-ply CFRP laminate (symmetric with of 0/90^{o}) was taken as Specimen II, which has the thickness of 3 mm and the same plane size (500 mm × 500 mm) with Specimen I. A square Teflon sheet was also inserted the between the interfaces of the second ply and the third ply, which has the same size (15 mm × 15 mm) and location (0.235 to 0.265 in ζ and 0.735 to 0.765 in η) with Specimen I. The same PZT actuator is mounted at the geometrical center of the front surface to generate harmonic

excitations. The natural frequency of Specimen II at 5309.37 Hz is arbitrarily selected as the excitation frequency. After laser scanning, corresponding SW with 371 × 371 measurement points is obtained and shown in figure 15(a), from which the DI is obtained and shown in figure 15(b). It can be seen from figure 15(b) that the location and size of the delamination can be graphically characterized as well as the results in figure 13 for Specimen I with different delamination depth.

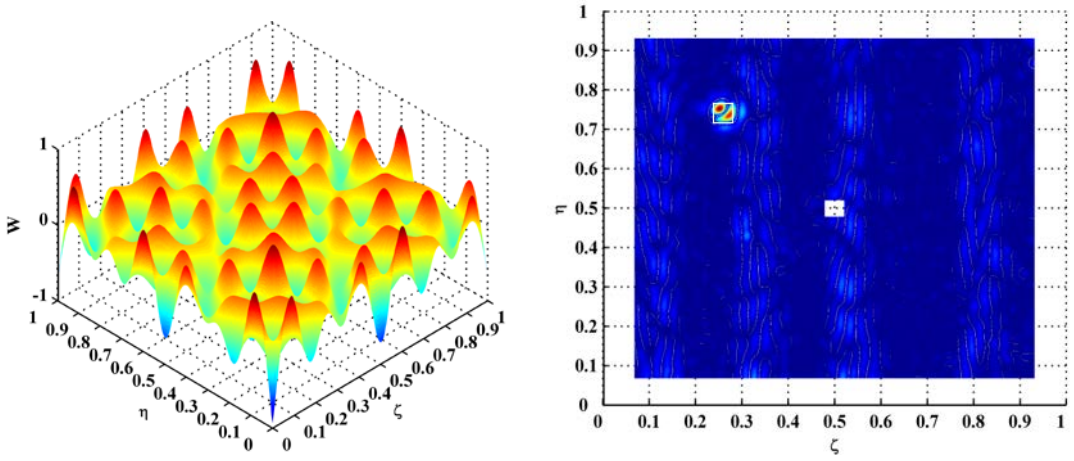

(a) (b)

Figure 15 (a) SW and (b) DI of Specimen II with the Teflon-caused delamination.

3.4 Experimental results for Specimen III

To validate the applicability of the approach to actual delamination that occur after manufacturing, a glass fiber reinforced polymer (GFRP) laminate is taken as Specimen III. The GFRP laminate has the lengths L_x and L_y of 440 mm in the *x*- and *y*-directions, respectively, and thickness h of 1.5 mm in the *z*-direction. The GFRP laminate consists of two plies whose fibers are oriented in the *x*-direction. The delamination was fabricated by heating the laminate in a local region using a hot air blower at the temperature of 500℃ for 6 seconds, by which the two plies instantly separate from each other in the heating region to form a delamination. The outline of the heating region is marked using a white ellipse, as shown in figure 16. Note that

Specimen III bears some barely visible original defects, the region of which is also marked using a white ellipse. The same PZT actuator is mounted at the geometrical center of the front surface of the specimen. The specimen is under a harmonic excitation at a natural frequency of 1264.0 Hz which is arbitrarily selected after modal analysis. After laser scanning, corresponding SW with 385 × 383 measurement points is obtained, as shown in figure 17(a). The DI is obtained from the SW and shown in figure 17(b), from which it can be seen that not only the delamination but also the original defects can be clearly imaged, locations and sizes of the detected delamination and original defects well corresponds to the actual damage regions enclosed by the ellipses. Note that the values of the DIs in figures 15(b) and 17(b) are vanished in the central regions, such that the effects of the excitations can be removed.

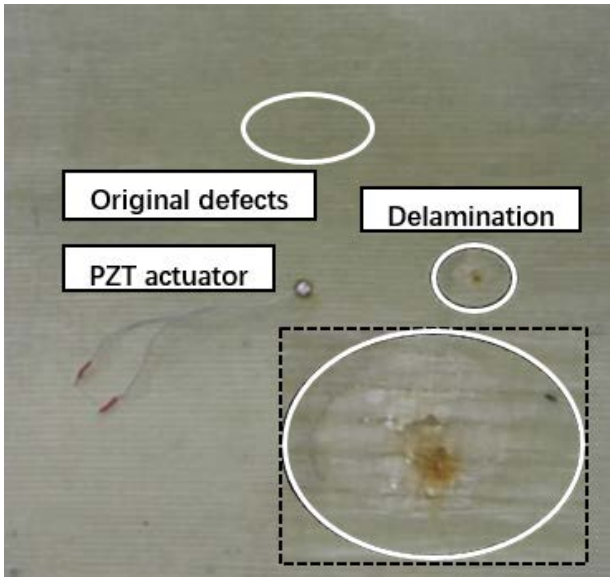

Figure 16 Specimen III with the heat-caused delamination.

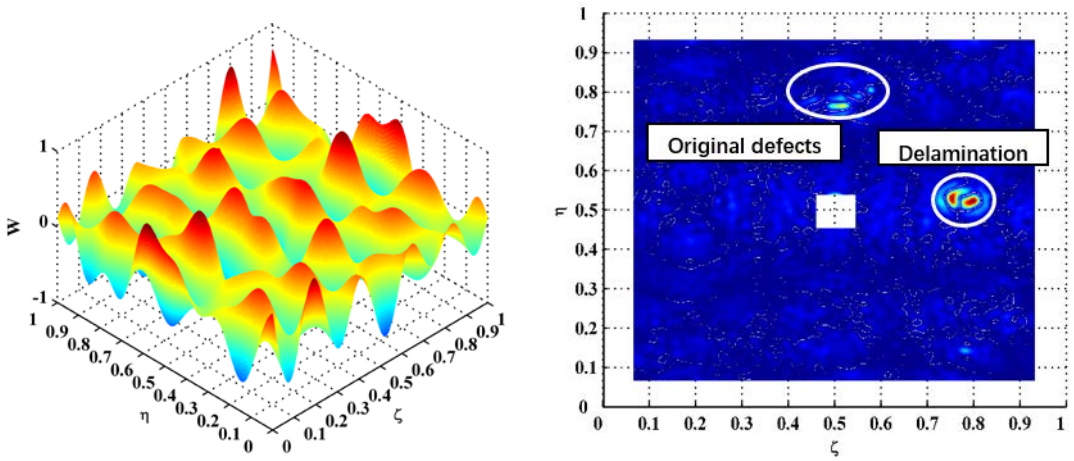

(a) (b)

Figure 17 (a) SW and (b) DI of Specimen III with the heat-caused delamination.

Although boundary conditions of the three specimens are all free, D-mode perturbation waves are independent of boundary conditions because they rapidly attenuate at undamaged locations including regions near boundaries. Therefore, the proposed approach is feasible to other boundary conditions. The computational efficiency of the proposed method is mainly determined by the multiscale analysis in equation (2). The computation was performed in Matlab using an ordinary desktop computer that has 16 GB of RAM and an Intel i7-9700 CPU with 8 cores. Computation of the multiscale analysis takes a dozen seconds which depends on the SW size and the rest computation takes less than one second. Therefore, the proposed approach requires low computational costs.

It is also noteworthy that for SW-based delamination imaging of built-up composite structures such as stiffened panels, effects of stringers [75-77] should be addressed in some future studies. Discontinuities of perturbation to SWs caused by delamination and stringers need be isolated. Besides, nonlinearities caused by interaction between interfaces of delamination [78-80] and artificial intelligence techniques [63-66] should also be addressed.

4 Concluding remarks

Delamination imaging is important for ensuring integrity and safety of laminated composite structures. Approaches for imaging delamination relying on wavefields have attracted increasing attention. This study proposes a novel imaging delamination approach using perturbation to SWs, by which delamination can be graphically characterized. Some conclusions are drawn as follows:

(1) This study extracts delamination-caused perturbation to a SW and proposes a new concept of delamination-caused perturbation wave, which is determined by delamination only and in a physical sense is naturally sensitive to delamination.

(2) The wavenumber analysis is applied to isolate D-mode and M-mode perturbation waves. In a physical sense, D-mode perturbation waves are generated by delamination, whereas the M-mode perturbation waves are “pseudo” waves caused by the manner of simplifying the stiffness coefficients. On the basis of D-mode perturbation waves, a DI is established for imaging delamination, by which the occurrence, location, and size of the delamination can be graphically characterized.

(3) The perturbation of a SW is estimated in a statistic manner without knowing structural and material parameters of composite laminates. Therefore, the approach proposed in this study for imaging delamination in composite laminates is baseline-free, which means that the material or structural parameters can be absent.

Acknowledgements

This work is supported by the Fundamental Research Funds for the Central Universities through Grant No. B210201034. Wei Xu is particularly grateful for the fellowship provided by the Hong Kong Scholars Program (No. XJ2018042). Maosen Cao, Zhongqing Su, and Hao Xu are grateful for the support from the National Natural Science Foundation of China through Grant Nos. 11772115, 51875492, and

12072056, respectively.

Nomenclature

$w(x, y, t)$	Waveform
$W(x, y)$	Steady-state wavefield
f_e	Harmonic excitation frequency
$\overline{\rho}$	Average density of composite laminate per unit area of midsurface
$\rho^{(d)}$	Density of the *d*th lamina per unit volume
$D_{ij}(x, y)$	Stiffness coefficients of composite laminate
$g(x, y)$	Gaussian function
$\overline{g}_s(x, y)$	Gaussian windowing function
$P(x, y)$	Perturbation to steady-state wavefield
$P^*(x, y)$	Normalized perturbation to steady-state wavefield
$P_D(x, y)$	Delamination-caused perturbation to steady-state wavefield
$P_D^*(x, y)$	Normalized delamination-caused perturbation to steady-state wavefield
$P_M(x, y)$	Material-caused perturbation to steady-state wavefield
$P_M^*(x, y)$	Normalized material-caused perturbation to steady-state wavefield
$\hat{P}^*(k_x, k_y)$	Wavenumber spectrum of perturbation to steady-state wavefield
k_x and k_y	Wavenumbers the *x*- and *y*-directions
$F(k_x, k_y)$	Low-pass wavenumber filter

$DI(x, y)$	Delamination index
L_x and L_y	Lengths of the CFRP laminate in the *x*- and *y*-directions
N_x and N_y	Sampling points of the CFRP laminate in each row and column in the *x*- and *y*-directions
h	Thickness of the CFRP laminate in the *z*-direction
K_x and K_y	Spatial sampling frequencies in the *x*- and *y*-directions

References:

[1] Lin X and Yuan F 2001 Damage detection of a plate using migration technique Journal of Intelligent *Journal of Intelligent Material Systems and Structures* 12(7) 469-482

[2] Staszewski W, Lee B, Mallet L and Scarpa F 2004 Structural health monitoring using scanning laser vibrometry: I. Lamb wave sensing *Smart Materials and Structures* 13(2) 251-260

[3] Mallet L, Lee B, Staszewski W and Scarpa F 2004 Structural health monitoring using scanning laser vibrometry: II. Lamb waves for damage detection *Smart Materials and Structures* 13(2) 261-269

[4] Leong W, Staszewski W, Lee B and Scarpa F 2005 Structural health monitoring using scanning laser vibrometry: III. Lamb waves for fatigue crack detection *Smart Materials and Structures* 14(6) 1387-1395

[5] Staszewski W, Lee B and Traynor R 2007 Fatigue crack detection in metallic structures with Lamb waves and 3D laser vibrometry *Measurement Science and Technology* 18(3) 727-739

[6] Ruzzene M 2007 Frequenc-wavenumber domain filtering for improved damage visualization *Smart Materials and Structures* 16(6) 2116-2129

[7] Ruzzene M, Xu B, Lee S, Michaels T and Michaels J 2010 Damage visualization via beamforming of frequency-wavenumber filtered wavefield data *Proceedings of SPIE, Health Monitoring of Structural and Biological Systems 2010,* 7650 76500L

[8] Radzienski M, Dolimski L, Krawczuk M, Zak A and Ostachowicz W 2011

Application of RMS for damage detection by guided elastic waves *Journal of Physics: Conference Series* 305(1) 012085

[9] Sohn H, Dutta D, Yang J, Desimio M, Olson S and Swenson E 2011 Automated detection of delamination and disbond from wavefield images obtained using a scanning laser vibrometer *Smart Materials and Structures* 20(4) 45017-45026

[10] Sohn H, Dutta D, Yang J, Park H, Desimio M, Olson S and Swenson E 2011 Delamination detection in composites through guided wave field image processing *Composites Science and Technology* 71(9) 1250-1256

[11] Michaels T, Michaels J and Ruzzene M 2011 Frequency-wavenumber domain analysis of guided wavefields *Ultrasonics* 51(4) 452-466

[12] Marchi L, Baravelli E, Ruzzene M, Speciale N and Masetti G 2012 Guided wave expansion in warped curvelet frames *IEEE Transactions on Ultrasonics, Ferroelectrics, and Frequency Control* 59(5) 949-957

[13] Rogge M and Johnston P 2012 Wavenumber imaging for damage detection and measurement *AIP Conference Proceedings* 1430 761

[14] Rogge M and Leckey C 2013 Characterization of impact damage in composite laminates using guided wavefield imaging and local wavenumber domain analysis *Ultrasonics* 53(7) 1217-1226

[15] Yu L and Tian Z 2013 Lamb wave structural health monitoring using a hybrid PZT-laser vibrometer approach *Structural Health Monitoring-An International Journal* 12(5-6) 469-483

[16] Flynn E and Jarmer G 2013 High-speed, non-contact, baseline-free imaging of

hiddden defects using scanning laser measurements of steady-state ultrasonic vibration *9th International Workshop on Structural Health Monitoring* Stanford, CA, USA

[17] Ostachowicz W, Radzienski M and Kudela P 2014 50th anniversary article: comparison studies of full wavefield signal processing for crack detection *Strain* 50(4) 275-291

[18] Flynn E 2014 Embedded multi-tone ultrasonic excitation and continuous-scanning laser Doppler vibrometry for rapid and remote imaging of structural defects *7th European Workshop on Structural Health Monitoring*, Nantes, France

[19] Tian Z, Leckey C, Seebo J and Yu L 2014 Guided wave delamination detection and quantification with wavefield data analysis *Proceedings of the ASME 2014 Conference on Smart Materials, Adaptive Structures and Intelligent Systems*, Newport, Rhode Island, USA

[20] An Y, Song H and Sohn H 2014 Wireless ultrasonic wavefield imaging via laser for hidden damage detection inside a steel box girder bridge *Smart Materials and Structures* 23(9) 095019

[21] Yu L, Tian Z and Leckey C 2015 Crack imaging and quantification in aluminum plates with guided wave wavenumber analysis methods *Ultrasonics* 62 203-212

[22] Tian Z, Yu L, Leckey C and Seebo J 2015 Guided wave imaging for detection and evaluation of impact-induced delamination in composites *Smart Materials and Structures* 24(10) 105019

[23] Kudela P, Radzienski M and Ostachowicz W 2015 Identification of cracks in thin-walled structures by means of wavenumber filtering *Mechanical Systems and Signal Processing* 50 456-466

[24] Mesnil O, Leckey C and Ruzzene M 2015 Instantaneous and local wavenumber estimations for damage quantification in composites *Structural Health Monitoring-An International Journal* 14(3) 193-204

[25] Juarez P and Leckey C 2015 Multi-frequency local wavenumber analysis and ply correlation of delamination damage *Ultrasonics* 62 56-65

[26] Jeon J, Gang S, Park G, Flynn E, Kang T and Han S 2017 Damage detection on composite structures with standing wave excitation and wavenumber analysis *Advanced Composite Materials* 26 53-65

[27] Michaels J 2017 Ultrasonic wavefield imaging: research tool or emerging NDE method? *AIP Conference Proceedings* 36 020001

[28] Williams W, Michaels T and Michaels J 2018 Application of wavefield imaging to characterize scattering from artificial and impact damage in composite laminate panels *AIP Conference Proceedings* 37 090007

[29] Esfandabadi Y, De Marchi L, Testoni N, Marzani A and Masetti G 2018 Full wavefield analysis and damage imaging through compressive sensing in Lamb wave inspections *IEEE Transactions on Ultrasonics, Ferroelectrics, and Frequency Control* 65(2) 269-280

[30] Kudela P, Radzienski M and Ostachowicz W 2018 Impact induced damage assessment by means of Lamb wave image processing *Mechanical Systems and*

Signal Processing 102 23-36

[31] Gan C, Chia C, Tan L, Mazlan N and Harley J 2018 Statistical evaluation of damage size based on amplitude mapping of damage-induced ultrasonic wavefield *IOP Conference Series: Materials Science and Engineering* 405 012006

[32] Yu L, Tian Z, Li X, Zhu R and Huang G 2019 Core-skin debonding detection in honeycomb sandwich structures through guided wave wavefield analysis *Journal of Intelligent Material Systems and Structures* 30(9) 1306-1317

[33] Esfandabadi Y, Bilodeau M, Masson P and De Marchi L 2019 Deep learning for enhancing wavefield image quality in fast non-contact inspections *Structural Health Monitoring-An International Journal* 19(4) 1003-1016

[34] Jeon J, Kim D, Park G, Flynn E, Kang T and Han S 2020 2D-wavelet wavenumber filtering for structural damage detection using full steady-state wavefield laser scanning *NDT&E International* 116 102343

[35] An Y, Park B and Sohn H 2013 Complete noncontact laser ultrasonic imaging for automated crack visualization in a plate *Smart Materials and Structures* 22(2) 025022

[36] Gao F, Shao Y, Hua J, Zeng L and Lin J 2021 Enhanced wavefield imaging method for impact damage detection in composite laminates via laser-generated Lamb waves *Measurement* 173 108639

[37] Lee J, Takatsubo J, Toyama N and Kang D 2007 Health monitoring of complex curved structures using an ultrasonic wavefield propagation imaging system *Measurement Science and Technology* 18(12) 3816-3824

[38] Lee J, Jeong H, Ciang C, Yoon D and Lee S 2010 Application of ultrasonic wave

propagation imaging method to automatic damage visualization of nuclear power plant pipeline *Nuclear Engineering and Design* 240(10) 3513-3520

[39] Lee J, Chia C, Shin H, Park C and Yoon D 2011 Laser ultrasonic propagation imaging method in the frequency domain based on wavelet transformation *Optics and Lasers in Engineering* 49(1) 167-175

[40] Flynn E, Chong S, Jarmer G and Lee J 2013 Structural imaging through local wavenumber estimation of guided waves *NDT&E International* 59 1-10

[41] An Y 2016 Impact-induced delamination detection of composites based on laser ultrasonic zero-lag cross-correlation imaging *Advances in Materials Science and Engineering* 2016 6474852

[42] Chang H and Yuan F 2019 Damage imaging in a stiffened curved composite sandwich panel with wavenumber index via Riesz transform *Structural Health Monitoring-An International Journal* 19(3) 902-916

[43] Wu Z, Chong S and Todd M 2020 Laser ultrasonic imaging of wavefield spatial gradients for damage detection *Structural Health Monitoring-An International Journal* 2020 doi: 10.1177/1475921720951336

[44] Chang H and Yuan F 2020 Visualization of hidden damage from scattered wavefield reconstructed using an integrated high-speed camera system *Structural Health Monitoring-An International Journal* 2020 doi: 10.1177/1475921720940805

[45] Alleyne D and Cawley P 1991 A two-dimensional Fourier transform method for the measurement of propagating multimode signals *The Journal of the Acoustical Society of America* 89(3) 1159-1168

[46] Zhu R, Huang G and Yuan F 2013 Fast damage imaging using the time-reversal technique in the frequency-wavenumber domain *Smart Materials and Structures* 22 075028

[47] Solodov I and Busse G 2007 Nonlinear air-coupled emission: The signature to reveal and image microdamage in solid materials *Applied Physics Letters* 91 251910

[48] Polimeno U and Meo M 2009 Detecting barely visible impact damage detection on aircraft composites structures *Composite Structures* 91 398-402

[49] Aymerich F and Staszewski W J 2010 Impact damage detection in composite laminates using nonlinear acoustics *Composites Part A: Applied Science and Manufacturing* 41 1084-1092

[50] Klepka A, Staszewski W J, di Maio D and Scarpa F 2013 Impact damage detection in composite chiral sandwich panels using nonlinear vibro-acoustic modulations *Smart Materials and Structures* 22 084011

[51] Pieczonka L, Ukowski P, Klepka A, Staszewski W J, Uhl T and Aymerich F 2014 Impact damage detection in light composite sandwich panels using piezo-based nonlinear vibro-acoustic modulations *Smart Materials and Structures* 23 105021

[52] Gaudenzi P, Nardi D, Chiappetta I, Atek S, Lampani L, Pasquali M, Sarasini F, Tirillo J and Valente T 2015 Sparse sensing detection of impact-induced delaminations in composite laminates *Composite Structures* 133 1209-1219

[53] Nardi D, Lampani L, Pasquali M and Gaudenzi P 2016 Detection of low-velocity impact-induced delaminations in composite laminates using Auto-Regressive models *Composite Structures* 151 108-113

[54] Solodov I, Bai J, Bekgulyan S and Busse G 2011 A local defect resonance to enhance acoustic wave-defect interaction in ultrasonic nondestructive evaluation *Applied Physics Letters* 99 211911

[55] Araújo dos Santos J V, Lopes H M R, Vaz M, Soares C M M, Soares C A M and De Freitas M J M 2006 Damage localization in laminated composite plates using mode shapes measured by pulsed TV holography *Composite Structures* 76 272-281

[56] Pérez M A, Gil L and Oller S 2014 Impact damage identification in composite laminates using vibration testing *Composite Structures* 108 267-276

[57] Xu W, Cao M S, Li X M, Radzieński M, Ostachowicz W and Bai R B 2017 Delamination monitoring in CFRP laminated plates under noisy conditions using complex-wavelet 2D curvature mode shapes *Smart Material and Structures* 26 104008

[58] Chen D M, Xu Y F and Zhu W D 2018 Non-model-based identification of delamination in laminated composite plates using a continuously scanning laser Doppler vibrometer system *Journal of Vibration and Acoustics* 140(4) 041001

[59] Xu W, Fang H, Cao M, Zhou L, Wang Q and Ostachowicz W 2019 A noise-robust damage indicator for characterizing singularity of mode shapes for incipient delamination identification in CFRP laminates *Mechanical Systems and Signal Processing* 121 183-200

[60] Xu W, Su Z, Liu J, Cao M S and Ostachowicz W 2020 Singular energy component for identification of initial delamination in CFRP laminates through piezoelectric actuation and non-contact measurement *Smart Materials and Structures*

29 045001

[61] Chandrashekhar M and Ganguli R 2016 Damage assessment of composite plate structures with material and measurement uncertainty *Mechanical Systems and Signal Processing* 75 75-93.

[62] Pérez M A, Pernas-Sánchez J, Artero-Guerrero J A and Serra-López R 2021 High-velocity ice impact damage quantification in composite laminates using a frequency domain-based correlation approach *Mechanical Systems and Signal Processing* 147 107124.

[63] Khan A and Kim H S 2018 Assessment of delaminated smart composite laminates via system identification and supervised learning *Composite Structures* 206: 354–362

[64] Khan A, Ko D K, Lim S C and Kim H S 2019 Structural Vibration-based classification and prediction of delamination in smart composite laminates using deep learning neural network *Composites Part B: Engineering* 161: 586–594

[65] Khan A, Kim N Y, Shin J K, Kim H S, and Youn B D 2019 A Damage assessment of smart composite structures via machine learning: a review *JMST Advances* 1: 107-124

[66] Khan A, Shin J K, Lim W C, Kim N Y and Kim H S 2020 A deep learning framework for vibration-based assessment of delamination in smart composite laminates *Sensors* 20: 2335

[67] Xu W, Zhu W D, Su Z, Cao M S and Xu H 2021 A novel structural damage identification approach using damage-induced perturbation in longitudinal vibration

Journal of Sound and Vibration 496 115932

[68] Mallat S 2008 A Wavelet Tour of Signal Processing *Academic Press*

[69] Leissa A and Qatu M 2011 Vibration of continuous systems *McGraw Hill*

[70] Zhao Y, Noori M, Altabey W, Ghiasi R and Wu Z 2019 A fatigue damage model for FRP composite laminate systems based on stiffness reduction *Structural Durability & Health Monitoring* 13 85-103

[71] Cao M S, Su Z, Xu H, Radzieński M, Xu W and Ostachowicz W 2020 A novel damage characterization approach for laminated composites in the absence of material and structural information *Mechanical Systems and Signal Processing* 143 106831

[72] Xu W, Zhu W D, Cao M S, Wu H and Zhu R 2020 A novel damage index for damage detection and localization of plate-type structures using twist derivatives of laser-measured mode shapes *Journal of Sound and Vibration* 481: 115448

[73] Yoon M K, Heider D, Gillespie J W, Ratcliffe C P and Crane R M 2005 Local damage detection using the two-dimensional gapped smoothing method *Journal of Sound and Vibration* 279(1-2): 119-139

[74] Xu H, Zeng Z, Wu Z, Zhou L, Su Z, Liao Y and Liu M 2017 Broadband dynamic responses of flexible carbon black/poly (vinylidene fluoride) nanocomposites: A sensitivity study *Composite Science and Technology* 149 246-253

[75] Sharif-Khodaei Z and Aliabadi M H 2014 Assessment of delay-and-sum algorithms for damage detection in aluminium and composite plates *Smart Materials and Structures* 23 075007

[76] Thiene M, Sharif-Khodaei Z and Aliabadi M H 2016 Optimal sensor placement

for maximum area coverage (MAC) for damage localization in composite structures *Smart Materials and Structures* 25 095037

[77] Yue N, Sharif-Khodaei Z and Aliabadi M H 2021 Damage detection in large composite stiffened panels based on a novel SHM building block philosophy *Smart Materials and Structures* 30: 045004

[78] Manoach E, Warminski J, Mitura A and Samborski S 2012 Dynamics of a composite Timoshenko beam with delamination *Mechanics Research Communications* 46 47-53

[79] Garcia D, Palazzetti R, Trendafilova I, Fiorini C and Zucchelli A 2015 Vibration-based delamination diagnosis and modelling for composite laminate plates *Composite Structures* 130 155-162

[80] Wang K, Liu M, Su Z, Guo S and Cui F 2021 Mode-mismatching enhanced disbond detection using material nonlinearity in guided waves at low frequency *Journal of Sound and Vibration* 490 115733